The Electrochemical Society
Advancing solid state & electrochemical science & technology

A Mass Transfer-Based Method for Controlled Electrosynthesis and Organization of Tetrathiafulvalene Bromide Micro/Nanowires

A Mass Transfer-Based Method for Controlled Electrosynthesis and Organization of Tetrathiafulvalene Bromide Micro/Nanowires

Disni Gunasekera,[1,=] Mohamed Kilani,[2,=] Xuecheng Yu,[2] Qianjin Chen,[3] Guangzhao Mao,[2,z] and Long Luo ●[1,*,z]

[1]*Department of Chemistry, Wayne State University, Detroit, Michigan 48202, USA*
[2]*Department of Chemical Engineering and Materials Science, Wayne State University, Detroit, Michigan 48202, USA*
[3]*College of Chemistry, Chemical Engineering and Biotechnology, Donghua University, Shanghai 201620, People's Republic of China*

Nanowire sensors are promising to deliver greater performance than conventional sensors due to their size confinement as well as low cost and power consumption. However, scalable assembly of nanowire sensors remains a big challenge, which requires the synthesis of uniform nanowires and organization of them. Here, we report a simple method to control the growth and organization of a promising nanowire material for gas sensing, tetrathiafulvalene bromide ((TTF)Br), by mass transfer in electrodeposition. We found that the use of Pt microdisk electrodes for electrodeposition of (TTF)Br wires resulted in wires with higher uniformity and larger aspect ratio (length to width) than their counterparts deposited on Pt films under the same deposition conditions. More interestingly, we found that the number of wires grown from a Pt microdisk electrode exhibited a limiting number of 3 or 4 per electrode when the electrode diameters are smaller than ∼1.4 μm. Both experimental and simulation results suggest that the morphological differences and the constant minimum wire density are caused by the different TTF flux distributions at a microdisk versus a film electrode. The results have significant implications for scalable manufacturing of nanowire-based sensing devices.
© 2019 The Electrochemical Society. [DOI: 10.1149/2.1001902jes]

One-dimensional nanostructures are widely recognized as the next generation building block for many chemical,[1–3] electronic,[4–6] and optical[7–9] applications on account of their unique physical and chemical properties. In particular, nanowire sensors are promising to deliver greater performances with size confinement as well as low cost and power consumption than conventional sensors.[10–14] Despite their attributes, nanowire sensors have yet to play a significant role in the sensing market. In 2016, the global nanosensors market was valued at $85 million[15] whereas the global market for sensors was $123.5 billion.[16] This is in part due to the lack of scalable manufacturing techniques to mass produce nanosensors. Fabrication of nanowire sensors typically goes through two steps: synthesis of nanowires and the subsequent device assembly. Recent advancements in synthetic methods make the scalable production of uniform nanowires possible. In contrast, scalable assembly of nanowire sensors remains a big challenge, which requires the nanowires to be organized over large areas with controlled orientation and density.[17] Several methods have been previously proposed to address this challenge, including using the electrical or magnetic field,[18,19] templates,[20] microfluidic flow,[21] layer-by-layer deposition,[22] optical trapping,[23] Langmuir-Blodgett technique,[24] and blown bubble film.[25] These methods, however, require multiple additional steps to align the wires prior to the sensor assembly. To further improve the efficiency of sensor manufacturing, it will be ideal if the synthesis of uniform wires and the organization of them can be accomplished in one single step.

Charge-transfer complexes are one promising group of materials for achieving this goal. These materials have been studied intensely in the last several decades mostly because of their one-dimensional growth and high conductivity.[26–30] We are interested in charge-transfer complexes for two main reasons: (1) their micro/nanowires can be synthesized directly on a device substrate via one-step electrochemical growth under ambient conditions,[31] which is difficult to realize for other one-dimensional materials such as metal or oxide nanowires; (2) we have recently discovered that charge-transfer complex wires, such as tetrathiafulvalene bromide ((TTF)Br) wires, show rapid and reversible conductivity changes in response to ammonia and other solvent vapors[1,32] making them potential materials for gas sensing applications.

Although the one-step electrochemical growth of charge-transfer complex wires on device substrates simplifies sensor fabrication

process, it is still challenging to control the uniformity, alignment, and density of these wires for scalable production. For example, we found that the (TTF)Br wires directly electrodeposited on a Pt film were randomly oriented and showed significant variations in length and width, which will be discussed in detail in the following sections. In this paper, we report a simple mass transfer-based method using microdisk electrodes (MDEs) to address this challenge. The benefits of using MDEs are four-fold: (1) unlike the transient mass transfer on a bulk electrode, the mass transfer on a MDE is at steady state ensuring the steady supply of reactants without significant fluctuations for uniform growth of the (TTF)Br wires; (2) the circular shape of MDEs creates a radial symmetry for growing radially oriented wires; (3) the non-uniform distribution of TTF flux across the surface of a MDE, where the flux at the periphery is higher than that close to the center, promotes one dimensional growth of the (TTF)Br wires leading to an increased aspect ratio (length to width); and (4) the number of wires per electrode can be conveniently adjusted by using MDEs of different sizes. This new method is important for the scalable fabrication of charge-transfer complex nanowire-based sensors.

Experimental

Chemicals and materials.—Tetrathiafulvalene (TTF, 97%), tetrabutylammonium bromide (TBABr, 98%), tetrabutylammonium hexafluorophosphate (TBAPF$_6$, 98%), and acetonitrile (ACN, 99.8%) were purchased from Sigma-Aldrich and used without further purification. Glass capillary (o.d./i.d.:1.65/1.10 mm; soft temperature: 785°C) was purchased from Dagan Corporation. Pt wire (25 μm diameter, 99.95%) was purchased from Alfa Aesar. W wire (250 μm diameter, 99.95%) were purchased from Solutions Materials. Pt film-coated Si wafer (SiO$_2$/Ti/Pt thin film on Si (100) (P-type) substrate, where the thickness of SiO$_2$, Ti, and Pt is 300 nm, 10 nm, and 150 nm, respectively) was purchased from MTI Corporation. SiC sandpapers were purchased from Buehler, and Ag conductive epoxy was purchased from MG Chemicals. All aqueous solutions were prepared from deionized (DI) water (PURELAB, 18.2 MΩ/cm, TOC < 3 ppb).

Fabrication of 25 μm diameter Pt microdisk electrodes.—A ∼2 cm long Pt microwire (25 μm in diameter) was attached to a W wire using Ag conductive epoxy. Then, the Pt wire was carefully inserted into a glass capillary followed by thermal sealing inside the capillary using an H$_2$/O$_2$ flame. The glass capillary with a sealed Pt microwire was polished using a SiC sandpaper until a Pt microdisk was exposed. Diameters of the prepared Pt microdisk electrodes (d_{Pt})
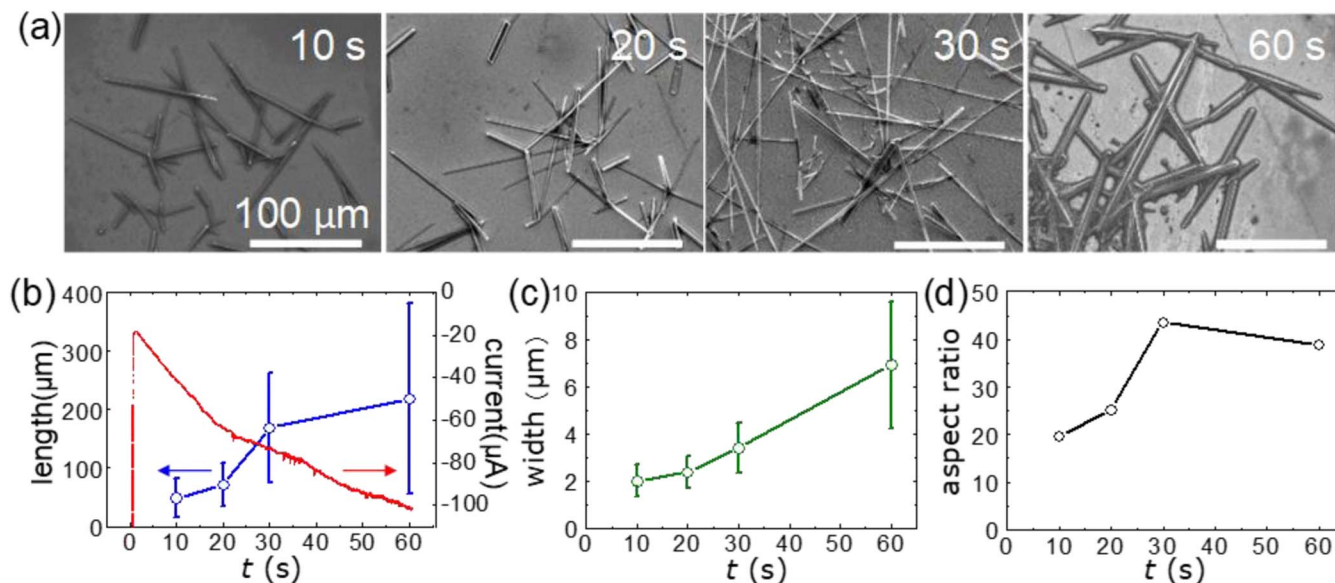
Figure 1. Electrodeposition of $(TTF)Br_{0.76}$ wires on a Pt film at 0.20 V vs Ag/AgCl in an ACN solution containing 5.0 mM TTF and 0.10 M TBABr. (a) SEM images of $(TTF)Br_{0.76}$ wires at deposition times of 10, 20, 30, and 60 s. (b) Plots of the average length of $(TTF)Br_{0.76}$ wires (blue) and anodic current (red) as a function of time (t). (c) Plot of the average width of $(TTF)Br_{0.76}$ wires vs t. (d) The average aspect ratio (length/width) of $(TTF)Br_{0.76}$ wires at different deposition times. The error bars in the graphs are the standard deviations of more than 30 wires.

were confirmed electrochemically by measuring the diffusion-limited current of these electrodes (i_{limit} in Figure S1) in an ACN electrolyte solution containing 5.0 mM TTF and 0.10 M $TBAPF_6$ using the following equation:[49]

$$i_{limit} = 2FC_{TTF}Dd_{Pt}$$

where $C_{TTF} = 5.0$ mM, D is the diffusion coefficient of TTF ($= 2.0 \times 10^{-5}$ cm^{2}s^{-1}),[48] and F is the Faraday constant.

Fabrication of Pt disk electrodes with diameters < 25 μm.—Pt disk electrodes with diameters < 25 μm were fabricated using a similar method as above.[52] The only difference is that prior to thermal sealing, the end of a Pt wire was sharpened in a 15 wt% $CaCl_2$ solution using a sinusoidal wave with 100 Hz frequency and $V_{app} = 4$ V. The average curvature of electrochemically sharpened Pt wire tips is ~20 nm. The Pt nanotip was cleaned using DI water and thermally sealed in a glass capillary. Pt electrodes with various diameters (from ~200 nm to 12 μm) were obtained by controlling the polishing time. The electrode diameters were electrochemically determined from the diffusion-limited current in 5.0 mM TTF in ACN using the same equation as above.

Electrochemistry.—All the electrochemical reactions were performed using the three-electrode system with a CHI potentiostat. Pt microdisk electrodes were used as working electrodes, and a 0.5 mm thick Pt wire was used as the counter electrode. An Ag/AgCl electrode in saturated KCl was used as the reference electrode because it has been reported to be one of the most stable reference electrodes in ACN solutions.[56]

SEM analysis.—The morphology of (TTF)Br wires was characterized by field-emission SEM (JEOL JSM 7600F SEM). The SEM including an in-lens thermo electron gun and a γ-filter for detection was operated at an acceleration voltage of 15 kV, working distance of 8 mm, and probe current of 6 μA. The ImageJ software was used for data analysis.

AFM.—The nanostructures of (TTF)Br wires were characterized by a Dimension 3100 AFM (Bruker) in the tapping mode under ambient conditions. The height, amplitude, and phase images were obtained using silicon tapping tips (nanoScience Instruments,

VistaProbes T300) with resonance frequency of 300 kHz and a nominal tip radius less than 30 nm. The images were analyzed using NanoScope Analysis 1.5 from Bruker.

Results and Discussion

Electrodeposition of (TTF)Br wires on a Pt film.—Electrodeposition of (TTF)Br on a Pt film electrode was carried out by applying an anodic potential step of 0.20 V vs Ag/AgCl in an ACN solution containing 5.0 mM TTF and 0.10 M TBABr for 10 to 60 s. At $E = 0.20$ V, TTF is oxidized to TTF^+ which then combines with Br^- to form randomly oriented (TTF)Br wires on the Pt film (Figure 1a). Note that although $E^{\circ}_{TTF^+/TFF} = 0.40$ V vs Ag/AgCl (Figure S1), the formation of insoluble (TTF)Br shifts the oxidation potential of TTF to more negative than 0.20 V. The wire morphology of (TTF)Br is primarily caused by its molecular structure, which defines the interfacial energies of different crystal facets.[33–36] The strong electrostatic bonding along the [001] direction is responsible for the faster growth rate of the (001) facet compared to the other facets, leading to the growth of wire-shaped crystals on the Pt film.[33] At electrode potentials more positive than 0.2 V, TTFBr exhibits featherlike morphologies as a result of the change of these interfacial energies (Figure S2). The (TTF)Br wires electrosynthesized under the above conditions are well known to be a mixed-valence salt, $(TTF)Br_x$, with the value of x ranging from 0.72 to 0.80 and an average reported value of 0.76.[37] The composition defines the extent of oxidation of the TTF chains, with the Br^- ions serving to neutralize the charge. Hereafter, we will use $(TTF)Br_{0.76}$ as the chemical formula of the electrodeposited (TTF)Br wires.

The chronoamperogram in Figure 1b (red curve) shows that the $(TTF)Br_{0.76}$ electrodeposition undergoes two stages. Initially, the current spikes to a large value (> 100 μA) followed by a quick (< 0.2 s) drop to a minimum current, i_{min}, of ~20 μA. After reaching i_{min}, the current increases nearly linearly with time (slope ~1.5 μA/s). A similar i-t behavior has been observed by Ward and coworkers in electrodeposition of $(TTF)Br_{0.76}$ on a gold electrode.[38,39] They attributed the initial current drop to two possible reasons. First, the $(TTF)Br_{0.76}$ nuclei cover the surface sufficiently so that their diffusion spheres merge and this results in the onset of planar or linear diffusion, similar to the Scharifker-Hills model for electrodeposition.[40–43] Second, the formation of inactive $(TTF)Br_{0.76}$ centers exhausts the energetically
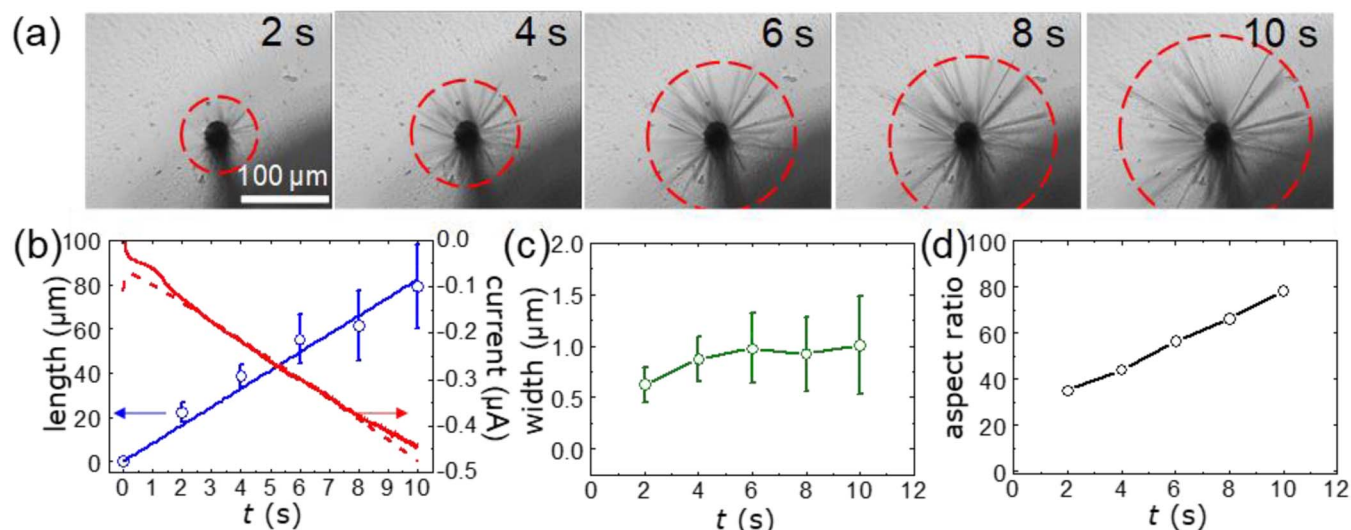
Figure 2. Electrodeposition of $(TTF)Br_{0.76}$ wires on a 25 μm diameter Pt MDE at 0.20 V vs Ag/AgCl in an ACN solution containing 5.0 mM TTF and 0.10 M TBABr. (a) Optical microscopic images of $(TTF)Br_{0.76}$ wires at deposition times of 2, 4, 6, 8, and 10 s. The dashed circles show the sizes of the $(TTF)Br_{0.76}$ wires-Pt MDE ensembles (TB-MDE). (b) The average length of $(TTF)Br_{0.76}$ wires (blue) and the current (red) vs t. The dashed red line shows the predicted i_{max} that is limited by the mass transfer of TTF to the electrode. (c) The average width and (d) aspect ratio of $(TTF)Br_{0.76}$ wires vs t. The error bars are the standard deviations of more than 30 wires.

favorable nucleation sites originally present on the gold electrode.[38] The current increase after i_{min} was caused by an increase in the effective electrode area due to the growth of conductive $(TTF)Br_{0.76}$ wires that behave as active electrode surfaces.[37,44]

Figures 1b and 1c show the average size of $(TTF)Br_{0.76}$ wires ranges from 44 μm at 10 s to 270 μm at 60 s in length, and from 2 μm at 10 s to 7 μm at 60 s in width, with a relative standard deviation of 30–65% and ∼34%, respectively. The large variation in length and width is most likely caused by the non-uniform distribution of $(TTF)Br_{0.76}$ nuclei on the electrode surface. For nuclei that are close to each other, they compete for the reagents and grow slowly, whereas nuclei that are further apart have less competition leading to faster growth.[42,45] The aspect ratio, defined as the ratio of the average length and width, increases at the beginning and reaches a maximum value of ∼40 after 30 s. The large variation in size, limited aspect ratio, and random orientation of the $(TTF)Br_{0.76}$ wires prepared by direct deposition on Pt films present the challenge in applying this electrochemical method for large-scale production of nanowire sensors, which demands a high degree of control over size, shape, orientation, and density of the nanowires.

Electrodeposition of $(TTF)Br_{0.76}$ wires on a Pt microdisk electrode (MDE).—To address the above challenge, we have found a simple but effective method to control the growth of $(TTF)Br_{0.76}$ wires using microdisk electrodes (MDEs). Figure 2a show the growth of $(TTF)Br_{0.76}$ wires from a 25 μm diameter Pt MDE at 0.20 V vs Ag/AgCl in an ACN solution of 5.0 mM TTF and 0.10 M TBABr. The nucleation sites of $(TTF)Br_{0.76}$ are randomly distributed on the electrode surface and the initial orientation of the wires is also random (Figure S3). At the initial growth stage (< 1 s), these wires on the MDE have already shown similar lengths and widths suggesting the nucleation of the wires occurred simultaneously. The wires grow radially with an average length of ∼80 μm after 10 s deposition and a constant growth rate of ∼8 μm/s (Figure 2b), which is ∼5 times that using a Pt film (∼1.5 μm/s). Moreover, these wires show a uniform length with a small relative standard deviation of < 25% (compared to 30–65% with the Pt film in Figure 1b). This small variation in length is not surprising because the disk geometry of the MDE provides a radial symmetry for the growth of $(TTF)Br_{0.76}$ wires. Most interestingly, the width of the wires reaches a constant value of ∼1 μm with a standard deviation of 24 to 48% (Figure 3c, and the corresponding SEM
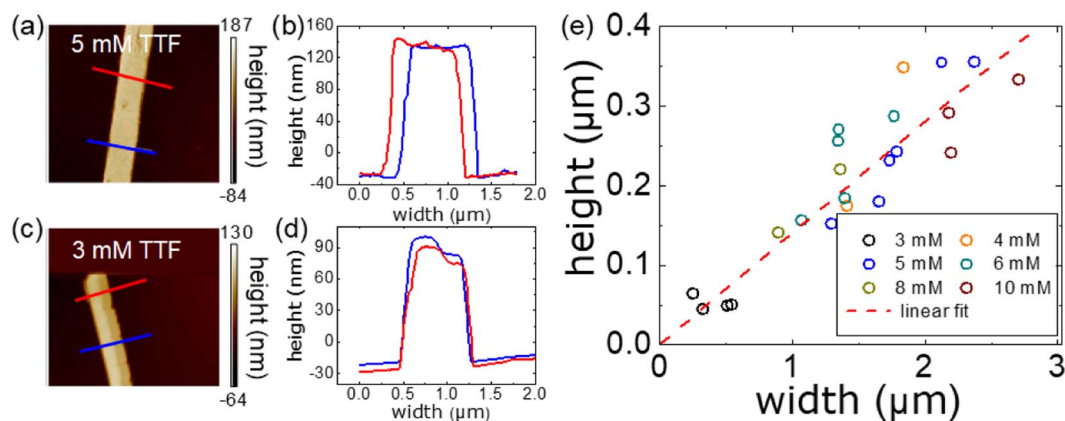
Figure 3. AFM cross-section analysis of $(TTF)Br_{0.76}$ wires that were grown using a 25 μm diameter Pt MDE at 0.20 V vs Ag/AgCl in ACN for 10 s. For (a) and (b), $C_{TTF} = 5.0$ mM and $C_{TBABr} = 0.10$ M; for (c) and (d), $C_{TTF} = 3.0$ mM and $C_{TBABr} = 0.10$ M. (e) The wire height vs width plot for $(TTF)Br_{0.76}$ wires grown at C_{TTF} from 3 to 10 mM. The red dashed line is the best linear fit of the data points with a slope of 0.14.
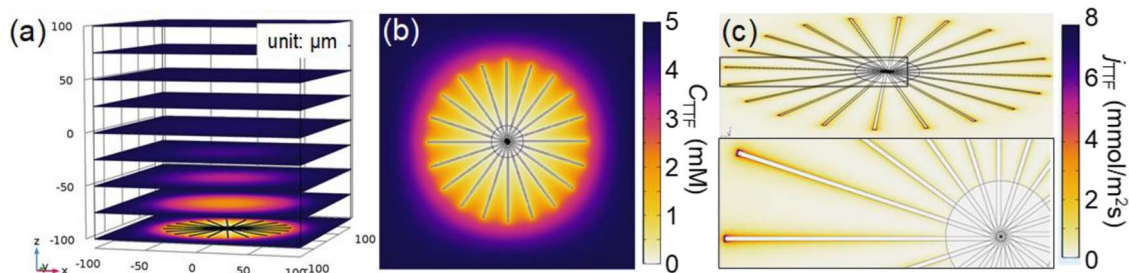
Figure 4. (a) Simulated steady-state C_{TTF} distributions on nine evenly-distributed xy planes at z values between -100 µm and 100 µm. The TB-MDE, which is located at $z = -100$ µm, comprises twenty (TTF)$Br_{0.76}$ wires (length: 50 µm, width: 1 µm, and height: 150 nm, corresponding to the wire morphology at a deposition time $= \sim 6$ s in Figure 2) connected to a 25 µm diameter disk. (b) Top view of the C_{TTF} distribution at the TB-MDE. The view dimension: 200 µm × 200 µm. (c) Distribution of the magnitude of total TTF flux (j_{TTF}) at the TB-MDE.

images are provided in Figure S2). As a result, the average aspect ratio of the (TTF)$Br_{0.76}$ wires increases linearly with electrodeposition time, reaching the value of 80 in 10 s (Figure 3d), which is ~ 4 times that of the wires grown on Pt films for the same duration (10 s) and ~ 2 times that of the maximum value on Pt films. We also tested the extended electrodeposition time up to 60 s for comparison with the wires grown on the Pt film. At 60 s, the average length, width and height of the wires reached 493.1, 5.9, and 2.0 µm, respectively (Figure S4a). During the entire 60 s, the wires kept growing longer. The average width, however, stayed at ~ 1 µm until 10 s, and then started to increase with a rate of ~ 0.1 µm/s (Figure S4c). Also, the wire width became non-uniform along the wires after 10s, with a larger width at the tip than that at the other end connected to the Pt-MDE (Figure S4b).

In addition to the length, width, and aspect ratio, we also found the cross-section profile of these wires to be slightly different from their counterparts on Pt films. Figure 3a shows a typical AFM image of the (TTF)$Br_{0.76}$ wires that were grown under the same conditions as in Figure 2. The height profiles of this wire (Figure 3b) show a uniform trapezoidal cross-section along the wire in agreement with the previously reported morphology.[33] The most prominent face is parallel to the substrate and extended along the needle axis of the wire. The widths of the top and bottom faces are ~ 0.6 µm and 1.0 µm, respectively, which are consistent with the average width measured by SEM (Figures 2c and S2). The wire height is ~ 170 nm leading to a height/width ratio of ~ 0.17 and a dihedral angle between the top and side faces of $\sim 120°$. Similar cross-section profiles are observed in (TTF)$Br_{0.76}$ wires that were prepared using other TTF concentrations during electrodeposition (Figures 3c and 3d). More interestingly, Figure 3e shows the height/width ratio for all wires is a constant of ~ 0.14 suggesting the side and top faces are at thermodynamic equilibrium.[46] In contrast, such a constant height/width ratio has not been previously observed for (TTF)$Br_{0.76}$ wires grown on planar electrodes, which exhibited a height/width ratio ranging from 0.2 to 0.5.[33] Overall, the simple change from Pt films to Pt MDEs results in radially oriented (TTF)$Br_{0.76}$ wires with a more uniform length, faster growth in the length direction than the width direction leading to a higher aspect ratio. These wires also show a relatively constant height/width ratio when grown on Pt MDEs.

Mechanism of morphological changes.—Thus far, we have described one interesting key finding: the use of Pt MDEs promotes the one-dimensional growth of the (TTF)$Br_{0.76}$ wires. To understand it, we first analyzed the *i-t* transient for the Pt MDE (Figure 2b) to determine the possible rate-determining step during the electrodeposition of (TTF)$Br_{0.76}$ wires. The *i-t* transient shows the current increases linearly with time. The increase in current is attributed to the growth of conductive (TTF)$Br_{0.76}$ wires, which expands the electroactive area for TTF oxidation.[38] To quantitatively interpret the linearity of the *i-t* trace, we estimate the current (i_{max}) that is limited by the mass transfer of TTF to the electrode using Eq. 1[47] by considering the Pt MDE and (TTF)$Br_{0.76}$ wires together as a new electrode with an increasing

diameter (denoted as TB-MDE).

$$i_{max} = i_{Cottrell} + i_{steady\ state}$$

$$= nFA(t)C_{TTF}\sqrt{\frac{D}{\pi t}} + 4nFDC_{TTF}(d_{Pt}/2 + L(t)) \quad [1]$$

where n is the number of charge transfer for oxidation of a TTF molecule ($n = 1$), F is the Faraday constant, $L(t)$ is the average length of (TTF)$Br_{0.76}$ wires as a function of time (t), d_{Pt} is the diameter of the Pt MDE ($d_{Pt} = 25$ µm), A is the electroactive area of the TB-MDE ($A = \pi(L + d_{Pt}/2)^2$), C_{TTF} is the bulk concentration of TTF, and D is the diffusion coefficient of TTF ($= 2.0 \times 10^{-5}$ cm^{2}s^{-1}).[48] The predicted i_{max} is plotted as a dashed red line in Figure 2b, which overlaps well with the experimental *i-t* trace. This agreement indicates that the TTF oxidation on TB-MDEs at 0.20 V is limited by the mass transfer of TTF to the electrode rather than the reaction kinetics. The specific contributions from the Cottrell ($i_{Cottrell}$) and steady-state terms ($i_{steady\ state}$) are provided in Figure S5. Because $i_{steady-state}$ accounts for more than 80% of the total current, we can approximately consider that the electrooxidation of TTF on the TB-MDE is at steady state for the entire 10 s deposition. Altogether, the TTF oxidation at a TB-MDE in our experiment was at steady state and limited by the mass transfer of TTF. Note that there are some slight deviations between the experimental and theoretical *i-t* traces before 2 s and after 8 s. The initial deviation may arise from the large contribution of TTF reactions on the MDE to the total current when wires are relatively short. The later deviation may be caused by the reduced overlap of diffusion layers on the periphery of TB-MDE as the spacing between the tips of wires increases. In both cases, the diffusional patterns of TTF are slightly different from that in our theoretical model.

Since mass transfer of TTF is the rate-determining step for generating TTF$^+$ and subsequent growth of (TTF)$Br_{0.76}$ wires, we hypothesize that the enhanced one-dimensional growth of (TTF)$Br_{0.76}$ wires (i.e., the increased length/width ratio) is caused by the TTF flux (j_{TTF}) distribution on the TB-MDE being different from that on a planar film. To test this hypothesis, we built a 3D steady-state finite element model to obtain the distribution of j_{TTF} at the TB-MDE during (TTF)$Br_{0.76}$ electrodeposition. Simulation details are provided in the SI (Figures S6 and S7). Briefly, we connect twenty (TTF)$Br_{0.76}$ wires (length: 50 µm, width: 1 µm, and height: 150 nm, corresponding to the wire morphology at a deposition time ~ 6 s in Figure 2) to a 25 µm diameter disk. For simplicity, we set the wires to be evenly distributed. As discussed above, electrooxidation of TTF is at steady state and limited by the mass transfer of TTF to the electrode, meaning $C_{TTF} = 0$ on the surfaces of (TTF)$Br_{0.76}$ wires and Pt MDE, both of which act as an active electrode (i.e., TB-MDE).

Figure 4a shows the simulated C_{TTF} distribution on different xy planes at z values from -100 µm to 100 µm. The diffusion layer thickness for TTF is ~ 100 µm, which is comparable to the size of TB-MDE. The C_{TTF} between (TTF)$Br_{0.76}$ wires is close to 0 (Figure 4b) indicating the diffusion layers for individual wires merge during
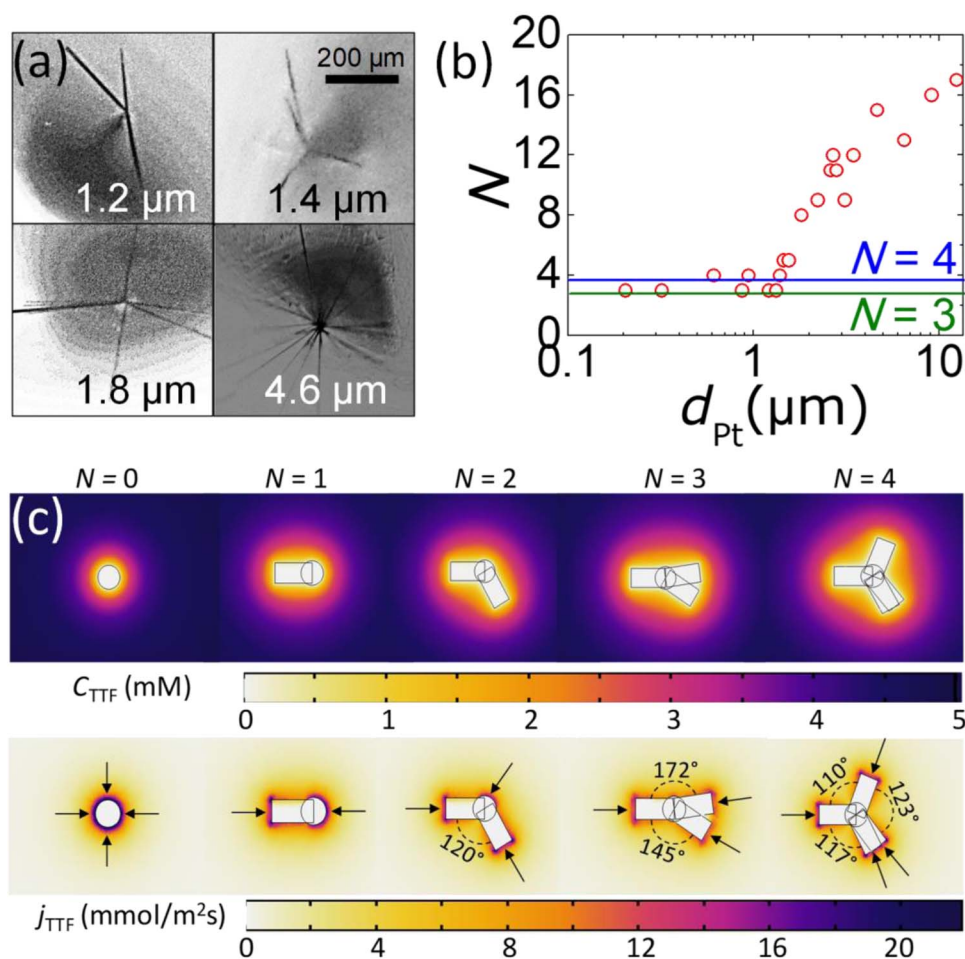
Figure 5. (a) Optical micrographs of (TTF)Br$_{0.76}$ wires grown using Pt disk electrodes with diameters (d_{Pt}) of 1.2, 1.4, 1.8, and 4.6 μm. The number of wires (N) increase from 3 to 15. Electrodeposition conditions: 0.20 V vs Ag/AgCl in an ACN with 5.0 mM TTF and 0.10 M TBABr for 10 s. (b) The plot of N vs d_{Pt} for 21 Pt disk electrodes with diameters from 200 nm to 12 μm. The lower limit of N is 3 or 4. (c) Top row: simulated C_{TTF} at a 1.2 μm diameter Pt disk electrode with different numbers of (TTF)Br$_{0.76}$ wires (N from 0 to 4). The wire length, width, and height are set as 2 μm, 1 μm, and 150 nm, respectively. For $N = 3$ and 4, the angles between wires were obtained from the micrographs in (a). Bottom row: simulated j_{TTF} distributions. The arrows indicate the regions with the largest j_{TTF}, or the "hot spots".

electrooxidation of TTF. This leads to a thicker diffusion layer near the center of the TB-MDE than on its periphery. Therefore, the j_{TTF} becomes much higher (> 6 times) at the tip of these (TTF)Br$_{0.76}$ wires than that along the body of these wires or at the Pt MDE (Figure 4c). Due to the steady-state condition, generation rate of TTF$^+$ is thus the highest at the wire tips. At $C_{TBABr} = 0.10$ M, Br$^-$ is in 20-fold excess, so TTF$^+$ ions are expected to completely react with Br$^-$ to form the building blocks for the (TTF)Br$_{0.76}$ wires. At the tip of a wire, there is a sufficient supply of building blocks for the fast growth of the (TTF)Br$_{0.76}$ wires. However, the lack of such supply along the body of these wires suppresses their growth in the width direction. The slow growth of the wire body leads to the establishment of a thermodynamic equilibrium between the top and side faces of the wires. In comparison, during electrodeposition of (TTF)Br$_{0.76}$ wire on a Pt film, j_{TTF} is relatively uniform across a Pt film (there is no higher j_{TTF} at the wire tip than on the wire body) due to the planar diffusion.[49] To conclude, the non-uniform distribution of j_{TTF} at the TB-MDE promotes one-dimensional growth of (TTF)Br$_{0.76}$ wires: enhanced growth in the length direction and suppressed growth in the width direction.

Controlling the density of (TTF)Br$_{0.76}$ wires.—In the previous sections, we have shown that the large j_{TTF} at the tips of (TTF)Br$_{0.76}$ wires promote their one-dimensional growth. Now, we continue to demonstrate the control of the density of (TTF)Br$_{0.76}$ wires. In this

experiment, we fabricated Pt disk electrodes with diameters from ~200 nm to 12 μm using a previously reported method[50–52] and used them to grow (TTF)Br$_{0.76}$ wires under the same deposition conditions as above: 10 s at 0.20 V vs Ag/AgCl in an ACN solution containing 5.0 mM TTF and 0.10 M TBABr. As shown in Figures 5a and 5b, the number of (TTF)Br$_{0.76}$ wires (N) grown using these Pt disk electrodes generally increases as the electrode diameter (d_{Pt}) increases. No meaningful correlation was observed between the electrode size and the dimensions of (TTF)Br$_{0.76}$ wires (Figure S8). The changed number of wires can be understood in terms of an increasing number of nucleation sites with increasing electrode size assuming a constant nucleation site density at all electrode sizes. Interestingly, however, we observed the existence of a lower limit of the number of wires to be 3–4 when the electrode size is reduced. All the electrodes with d_{Pt} < 1.4 μm grow either 3 or 4 wires (Figures 5b and S9).

This lower limit is surprising because a single nucleation site is commonly observed when an electrode approaches nanometer dimensions.[40,53–55] It might arise from the nucleus having a particular crystal structure with 3 or 4 most favorable facets for wire growth. However, if it is true, when we deposited these wires using a Pt film, we should have observed similar (TTF)Br$_{0.76}$ wire ensembles, each containing 3 or 4 wires, rather than the relatively independent individual wires in Figure 1. This discrepancy leads to another possible mechanism: the local j_{TTF} affects the initial growth of (TTF)Br$_{0.76}$ wires from a nucleus. As discussed in previous sections, the

elongation of $(TTF)Br_{0.76}$ wires is accelerated by a high local j_{TTF}. By analogy, it is likely that the high local j_{TTF} can also help with the initial growth of $(TTF)Br_{0.76}$ wires from a nucleus. Figure 5c shows the simulated C_{TTF} and j_{TTF} distributions at a 1.2 μm diameter Pt disk electrode with different numbers of $(TTF)Br_{0.76}$ wires attached (N from 0 to 4). At $N = 0$, the j_{TTF} is axisymmetric around the disk electrode, so there is no location with larger j_{TTF} (or the "hot spot"). At $N = 1$ and 2, the hot spots are located at the tips of the wires as well as part of the disk electrode edge as indicated by the arrows. The latter one might promote the growth of additional wires from the nucleus at the Pt disk electrode causing $N = 1$ and 2 not favored. At $N = 3$ and 4, however, the hot spots are only present at the tips of the wires, so they are not able to assist in the growth of new wires. For larger electrodes (>1.4 μm), when $N = 3$ and 4, the hot spots are, however, located all around the disk electrode rather than just on the tips of the wires, resulting in the nucleation of additional wires (> 4 wires) on the electrode surface (Figure S10). Hence, $N = 3$ or 4 becomes the minimum wire density that can be achieved by reducing electrode size.

Conclusions

In conclusion, we have demonstrated a simple but effective method to control the growth of $(TTF)Br_{0.76}$ micro/nanowires using microelectrodes. The use of Pt MDEs ameliorates the uniformity of $(TTF)Br_{0.76}$ wires with a relative length standard deviation of less than 25% compared to 30–65% for a Pt film. In addition, the elongation of the wires becomes ∼5 times faster than that using a Pt film, while their widths remain relatively constant during the growth overcoming the aspect ratio of ∼40 that were found in the $(TTF)Br_{0.76}$ wires grown on Pt films. The AFM cross-section profiling result shows a constant height/width ratio of ∼0.14 for all wires grown using Pt MDEs, suggesting the top and side faces of these wires are at thermodynamic equilibrium. Analysis of the i-t transient during electrodeposition reveals the rate determining step for the wire growth is the mass transfer of TTF to the electrode. The fast mass transfer rate at the tips of the TTF wires grown from a Pt MDE promotes the one-dimensional growth. We also discovered that the number of wires per electrode depends on the size of the Pt MDE and exhibits an unusual minimum of 3 or 4 per electrode for $d_{Pt} <1.4$ μm. This lower limit of wire numbers can be explained by the dependence of TTF flux distribution on the number of wires grown out from a Pt MDE. Nanowires with high aspect ratios will provide high sensitivity in nanowire sensors. The use of charge-transfer salts could potentially enhance sensor selectivity without the need for further surface functionalization. These features enable us to move closer toward the realization of a low-cost and scalable manufacturing technique of nanowire chemical sensors. This technique has the potential of being a reliable platform for the manufacturing of micro/nanowire-based devices such as FET transistors, electronic interconnects, and quantum gates.

Acknowledgments

ORCID

Long Luo   https://orcid.org/0000-0001-5771-6892

References

1. P. Jahanian, X. C. Yu, M. Kilani, and G. Z. Mao, "Electrodeposition of Partially Oxidized Tetracyanoplatinate Nanowires on Seeds and Patterns for Gas Sensing." *Mater. Res. Lett.*, **5**(8), 569 (2017).
2. A. Lichtenstein, E. Havivi, R. Shacham, E. Hahamy, R. Leibovich, A. Pevzner, V. Krivitsky, G. Davivi, I. Presman, R. Elnathan, Y. Engel, E. Flaxer, and F. Patolsky, "Supersensitive Fingerprinting of Explosives by Chemically Modified Nanosensors Arrays." *Nat. Commun.*, **5**, 4195 (2014).
3. D. Liu, L. M. Lin, Q. F. Chen, H. Z. Zhou, and J. M. Wu, "Low Power Consumption Gas Sensor Created from Silicon Nanowires/TiO2 Core-Shell Heterojunctions." *ACS Sens.*, **2**(10), 1491 (2017).
4. D. H. Kim, J. H. Ahn, W. M. Choi, H. S. Kim, T. H. Kim, J. Z. Song, Y. G. Y. Huang, Z. J. Liu, C. Lu, and J. A. Rogers, "Stretchable and Foldable Silicon Integrated Circuits." *Science*, **320**(5875), 507 (2008).
5. S. Y. Min, T. S. Kim, B. J. Kim, H. Cho, Y. Y. Noh, H. Yang, J. H. Cho, and T. W. Lee, "Large-Scale Organic Nanowire Lithography and Electronics." *Nat. Commun.*, **4**, 1773 (2013).
6. T. Sekitani, Y. Noguchi, K. Hata, T. Fukushima, T. Aida, and T. Someya, "A Rubber-like Stretchable Active Matrix Using Elastic Conductors." *Science*, **321**(5895), 1468 (2008).
7. X. F. Duan, Y. Huang, R. Agarwal, and C. M. Lieber, "Single-Nanowire Electrically Driven Lasers." *Nature*, **421**(6920), 241 (2003).
8. X. F. Duan, Y. Huang, Y. Cui, J. F. Wang, and C. M. Lieber, "Indium Phosphide Nanowires as Building Blocks for Nanoscale Electronic and Optoelectronic Devices." *Nature*, **409**(6816), 66 (2001).
9. M. S. Gudiksen, L. J. Lauhon, J. Wang, D. C. Smith, and C. M. Lieber, "Growth of Nanowire Superlattice Structures for Nanoscale Photonics and Electronics." *Nature*, **415**(6872), 617 (2002).
10. R. M. Penner, "Chemical Sensing with Nanowires." *Annu. Rev. Anal. Chem.*, **5**, 461 (2012).
11. Z. L. Wang, "Self-Powered Nanosensors and Nanosystems." *Adv. Mater.*, **24**(2), 280 (2012).
12. J. Yun, J. H. Ahn, Y. K. Choi, and I. Park, "Ultra-Low Power Hydrogen Sensor by Suspended and Palladium Coated Silicon Nanowire." *30th IEEE International Conference on Micro Electro Mechanical Systems (Mems 2017)*, 1079 (2017).
13. R. Shimotsu, T. Takumi, and V. Vohra, "All Solution-Processed Micro-Structured Flexible Electrodes for Low-Cost Light-Emitting Pressure Sensors Fabrication." *Sci. Rep.*, **7**, 6921 (2017).
14. J. F. Fennell, S. F. Liu, J. M. Azzarelli, J. G. Weis, S. Rochat, K. A. Mirica, J. B. Ravnsbaek, and T. M. Swager, "Nanowire Chemical/Biological Sensors: Status and a Roadmap for the Future." *Angew Chem Int Edit*, **55**(4), 1266 (2016).
15. Nanosensors Market. https://www.variantmarketresearch.com/report-categories/semiconductor-electronics/nanosensors-market (accessed January 2018).
16. S. Smith, Global Markets and Technologies for Sensors. https://www.prnewswire.com/news-releases/global-markets-and-technologies-for-sensors-300430105.html (accessed March 27, 2017).
17. "A Matter of Scale." *Nat. Nanotechnol.*, **11**(9), 733 (2016).
18. P. A. Smith, C. D. Nordquist, T. N. Jackson, T. S. Mayer, B. R. Martin, J. Mbindyo, and T. E. Mallouk, "Electric-Field Assisted Assembly and Alignment of Metallic Nanowires." *Appl. Phys. Lett.*, **77**(9), 1399 (2000).
19. C. M. Hangarter and N. V. Myung, "Magnetic Alignment of Nanowires." *Chem. Mater.*, **17**(6), 1320 (2005).
20. M. Friedl, K. Cerveny, P. Weigele, G. Tutuncuoglu, S. Marti-Sanchez, C. Y. Huang, T. Patlatiuk, H. Potts, Z. Y. Sun, M. O. Hill, L. Guniat, W. Kim, M. Zamani, V. G. Dubrovskii, J. Arbiol, L. J. Lauhon, D. M. Zumbuhl, and A. F. I. Morral, "Template-Assisted Scalable Nanowire Networks." *Nano Lett.*, **18**(4), 2666 (2018).
21. K. Oh, J. H. Chung, J. J. Riley, Y. L. Liu, and W. K. Liu, "Fluid Flow-Assisted Dielectrophoretic Assembly of Nanowires." *Langmuir*, **23**(23), 11932 (2007).
22. A. Javey, S. Nam, R. S. Friedman, H. Yan, and C. M. Lieber, "Layer-By-Layer Assembly of Nanowires for Three-Dimensional, Multifunctional Electronics." *Nano Lett.*, **7**(3), 773 (2007).
23. P. J. Pauzauskie, A. Radenovic, E. Trepagnier, H. Shroff, P. D. Yang, and J. Liphardt, "Optical Trapping and Integration of Semiconductor Nanowire Assemblies in Water." *Nat. Mater.*, **5**(2), 97 (2006).
24. L. Q. Mai, Y. H. Gu, C. H. Han, B. Hu, W. Chen, P. C. Zhang, L. Xu, W. L. Guo, and Y. Dai, "Orientated Langmuir-Blodgett Assembly of VO2 Nanowires." *Nano Lett.*, **9**(2), 826 (2009).
25. G. H. Yu, A. Y. Cao, and C. M. Lieber, "Large-Area Blown Bubble Films of Aligned Nanowires and Carbon Nanotubes." *Nat. Nanotechnol.*, **2**(6), 372 (2007).
26. K. P. Goetz, D. Vermeulen, M. E. Payne, C. Kloc, L. E. McNeil, and O. D. Jurchescu, "Charge-Transfer Complexes: New Perspectives on an Old Class of Compounds." *J. Mater. Chem. C*, **2**(17), 3065 (2014).
27. L. Ren, X. J. Xian, K. Yan, L. Fu, Y. W. Liu, S. L. Chen, and Z. F. Liu, "A General Electrochemical Strategy for Synthesizing Charge-Transfer Complex Micro/Nanowires." *Adv. Funct. Mater.*, **20**(8), 1209 (2010).
28. D. M. Ivory, G. G. Miller, J. M. Sowa, L. W. Shacklette, R. R. Chance, and R. H. Baughman, "Highly Conducting Charge-Transfer Complexes of Poly(Para-Phenylene)." *J. Chem. Phys.*, **71**(3), 1506 (1979).
29. R. Basori and A. K. Raychaudhuri, "Low Temperature Transport of a Charge Transfer Complex Nanowire Grown with an Electric Field from the Vapour Phase." *Rsc Adv.*, **5**(105), 86497 (2015).
30. D. L. Wang, X. L. Qiao, J. W. Tao, Y. Zou, H. Z. Wu, D. B. Zhu, and H. X. Li, "Cu-Thienoquinone Charge-Transfer Complex: Synthesis, Characterization, and Application in Organic Transistors." *ACS Appl. Mater. Inter.*, **10**(31), 26451 (2018).
31. F. B. Kaufman, E. M. Engler, D. C. Green, and J. Q. Chambers, "Electrochemical Preparation and Control of Stoichiometry for Donor-Halide Salts - TTFX$_n$ and TSeFX$_n$." *J. Am. Chem. Soc.*, **98**(6), 1596 (1976).
32. G Mao, Electrochemical Deposition of Nanowires on Nanoparticles, Lithographical Patterns and Electronic Devices and Their Use as Chemical Sensors. U.S. Pat. 20180128776, May 10, 2018.

33. A. C. Hillier and M. D. Ward, "Atomic-Force Microscopy of the Electrochemical Nucleation and Growth of Molecular-Crystals." *Science*, **263**(5151), 1261 (1994).
34. L. Li, P. Jahanian, and G. Z. Mao, "Electrocrystallization of Tetrathiafulvalene Charge-Transfer Salt Nanorods on Gold Nanoparticle Seeds." *J. Phys. Chem. C*, **118**(32), 18771 (2014).
35. M. Mas-Torrent and P. Hadley, "Electrochemical Growth of Organic Conducting Microcrystals of Tetrathiafulvalene Bromide." *Small*, **1**(8–9), 806 (2005).
36. M. D. Ward, "Electrocrystallization of Low Dimensional Solids - Directed Selectivity and Investigations of Crystal-Growth with the Quartz Crystal Microbalance." *Synth. Met.*, **27**(3–4), B211 (1988).
37. B. A. Scott, S. J. Laplaca, J. B. Torrance, B. D. Silverman, and B. Welber, "Crystal-Chemistry of Organic Metals - Composition, Structure, and Stability in Tetrathiofulvalinium-Halide Systems." *J. Am. Chem. Soc.*, **99**(20), 6631 (1977).
38. M. D. Ward, "Probing Electrocrystallization of Charge-Transfer Salts with the Quartz Crystal Microbalance." *J. Electroanal. Chem.*, **273**(1–2), 79 (1989).
39. B. A. Scott, S. J. LaPlaca, J. B. Torrance, B. D. Silverman, and B. Welber, "Crystal Chemistry of Mixed-Valence TTF Salts." *Ann. N.Y. Acad. Sci.*, **313**(1), 369 (1978).
40. S. C. S. Lai, R. A. Lazenby, P. M. Kirkman, and P. R. Unwin, "Nucleation, Aggregative Growth and Detachment of Metal Nanoparticles During Electrodeposition at Electrode Surfaces." *Chem. Sci.*, **6**(2), 1126 (2015).
41. G. Hills, I. Montenegro, and B. Scharifker, "3-Dimensional Nucleation of Lead." *J. Appl. Electrochem.*, **10**(6), 807 (1980).
42. B. Scharifker and G. Hills, "Theoretical and Experimental Studies of Multiple Nucleation." *Electrochim. Acta*, **28**(7), 879 (1983).
43. D. Grujicic and B. Pesic, "Electrodeposition of Copper: the Nucleation Mechanisms." *Electrochim. Acta*, **47**(18), 2901 (2002).
44. P. Kathirgamanathan and D. R. Rosseinsky, "Novel Conductive Adducts of Tetrathiafulvalene and Tetrathiatetracene." *J. Chem. Soc., Chem. Commun.*, (8), 356 (1980).
45. F. Favier, H. T. Liu, and R. M. Penner, "Size-Selective Growth of Nanoscale Tetrathiafulvalene Bromide Crystallites on Platinum Particles." *Adv. Mater.*, **13**(20), 1567 (2001).
46. G. Wulff, "On The Question of Speed of Growth and Dissolution of Crystal Surfaces." *Z. Kristallogr.*, **34**(5/6), 449 (1901).
47. Z. G. Soos and P. J. Lingane, "Derivation of Chronoamperometric Constant for Unshielded Circular Planar Electrodes." *J. Phys. Chem.*, **68**(12), 3821 (1964).
48. T. H. Y. Ha, K. Rasmussen, S. Landgraf, and G. Grampp, "Diffusion of Tetrathiafulvalene and Its Radical Cation in Ionic Liquids in Comparison to Conventional Solvents." *Electrochim. Acta*, **141**, 72 (2014).
49. A. Bard and L. Faulkner, "Mass Transfer by Migration and Diffusion." In *Electrochemical Methods: Fundamentals and Applications*, John Wiley & Sons, Inc: 2001; pp 161.
50. Q. J. Chen and L. Luo, "Correlation between Gas Bubble Formation and Hydrogen Evolution Reaction Kinetics at Nanoelectrodes." *Langmuir*, **34**(15), 4554 (2018).
51. Q. J. Chen, R. Ranaweera, and L. Luo, "Hydrogen Bubble Formation at Hydrogen-Insertion Electrodes." *J. Phys. Chem. C*, **122**(27), 15421 (2018).
52. B. Zhang, J. Galusha, P. G. Shiozawa, G. L. Wang, A. J. Bergren, R. M. Jones, R. J. White, E. N. Ervin, C. C. Cauley, and H. S. White, "Bench-Top Method for Fabricating Glass-Sealed Nanodisk Electrodes, Glass Nanopore Electrodes, and Glass Nanopore Membranes of Controlled Size." *Anal. Chem.*, **79**(13), 4778 (2007).
53. J. Velmurugan, J. M. Noel, W. Nogala, and M. V. Mirkin, "Nucleation and Growth of Metal on Nanoelectrodes." *Chem. Sci.*, **3**(11), 3307 (2012).
54. K. Huang, J. Clausmeyer, L. Luo, K. Jarvis, and R. M. Crooks, "Shape-Controlled Electrodeposition of Single Pt Nanocrystals Onto Carbon Nanoelectrodes." *Faraday Discuss.*, **210**(0), 267 (2018).
55. J. Velmurugan and M. V. Mirkin, "Fabrication of Nanoelectrodes and Metal Clusters by Electrodeposition." *Chemphyschem*, **11**(13), 3011 (2010).
56. Overview of Reference Electrodes and Alternative Reference Electrodes. https://www.pineresearch.com/shop/wp-content/uploads/sites/2/2016/10/DRK10053 -Overview-of-Reference-Electrode-Operation-and-Alternative-Reference-Electrodes -REV001.pdf (accessed April 2016).